NUMERICAL SIMULATIONS ON HEAT FLOW VISUALIZATION AND ENTROPY GENERATION DURING NATURAL CONVECTION IN ENCLOSURES WITH CURVED SIDE WALLS

Biswal P. and Basak T.*

*Author for correspondence
Department of Chemical Engineering,
Indian Institute of Technology Madras,
Chennai - 600036, India
Email: tanmay@iitm.ac.in

ABSTRACT

In the present work, investigation of heat flow via heatlines in addition to entropy generation due to natural convection within differentially heated cavities with curved side walls is carried out. Galerkin finite element method with penalty parameter is used to solve the nonlinear coupled partial differential equations governing the flow and thermal fields and the finite element method is further used to solve the Poisson equation for streamfunction and heatfunction. The derivative terms in the expression of entropy generation is calculated using the elemental basis sets. Numerical simulations are carried out for a range of Rayleigh numbers ($Ra = 10^3$-10^5) and the Prandtl number, $Pr = 0.01$. The results are elucidated in terms of streamlines, heatlines and isotherms to present the heat flow patterns in the cavity. A comprehensive understanding on internal convective heat flow is illustrated using heatline concept. Entropy generation due to heat transfer and fluid friction are also illustrated concave and convex cases. Based on high heat transfer rate and lesser total entropy generation, case 3 (highly concave) may be chosen over cases 1 (less concave) and 2 (moderate concave) for all Ra. Similarly, in convex cases, case 1 with less convexity offers higher heat transfer rate with less entropy generation compared to that of cases 2 (moderate convex) and 3 (highly convex).

INTRODUCTION

Natural convection heat flow in enclosures is frequently encountered in various engineering and industrial applications such as, building and ventilation, cooling of electronic chips, thermal storage tanks, food storage, solar collectors etc. Thus, investigation of natural convection in confined cavities with various geometric configurations is important in thermal processing. Thus, a number of studies on natural convections have been carried out by researchers since last few decades. However, in many earlier studies, the fluid flow visualization via streamlines and temperature distribution are given much importance while the thermal management in heat flow is not addressed properly. In order to understand the trajectory of heat flow and heat distribution, one has to study the heatlines. The basic concept of heatline was first introduced by Kimura and Bejan [1]. Following Kimura and Bejan [1], many works on analysis of heatlines are also carried out by researchers [2, 3, 4, 5, 6]. However, heatlines are not adequate to explain losses of energy or efficiency of heating processes during convection. Consequently, analysis of entropy generation can be carried out to understand the efficiency of the heating process as the loss in available energy is directly proportional to the entropy generation. Bejan [7] introduced entropy generation minimization concept based on the second law of thermodynamics. Many studies on entropy generation during natural convection in enclosures with various shapes are found in the literature [8, 9, 10].

The main objective of the present study is to analyze the effect of wall curvature on the characteristics of heat flow, fluid flow and entropy generation due to heat transfer and fluid friction during natural convection within a complex cavity with curved side walls. The enclosure is bounded by horizontal adiabatic walls with hot left and cold right walls [see Figure 1]. Numerical simulations were carried out for various Rayleigh numbers ($Ra = 10^3 - 10^5$), at $Pr = 0.01$. Galerkin finite element method [11] with a penalty parameter is used in order to solve the non-linear partial differential equations.

NOMENCLATURE

g	[m s^{-2}]	acceleration due to gravity
L	[m]	height of enclosure
N	[-]	total number of nodes
Nu	[-]	local Nusselt number
$\overline{Nu}$	[-]	average Nusselt number
p	[Pa]	pressure
P	[-]	dimensionless pressure
Pr	[-]	Prandtl number
R	[-]	Residual of weak form
Ra	[-]	Rayleigh number
S	[-]	dimensionless distance along the wall
S_{max}	[-]	length of the curved wall
s'	[-]	dummy variable
T	[K]	temperature
T_h	[K]	temperature of hot right wall

T_c	[K]	temperature of cold left wall
u	[m s^{-1}]	x component of velocity
U	[-]	x component of dimensionless velocity
v	[m s^{-1}]	y component of velocity
V	[-]	y component of dimensionless velocity
x	[m]	distance along x coordinate
X	[-]	dimensionless distance along x coordinate
y	[m]	distance along y coordinate
Y	[-]	dimensionless distance along y coordinate

Greek symbols

α	[m^2 s^{-1}]	thermal diffusivity
β	[K^{-1}]	volume expansion coefficient
γ	[-]	penalty parameter
θ	[-]	dimensionless temperature
ν	[m^2 s^{-1}]	kinematic viscosity
ρ	[kg m^{-3}]	density
Φ	[-]	basis functions
Π	[-]	dimensionless heatfunction
φ	[-]	angle made by tangent of curved wall with positive x axis
ψ	[-]	dimensionless streamfunction
Ω	[-]	two dimensional domain
ξ	[-]	horizontal coordinate in a unit square
η	[-]	vertical coordinate in a unit square

Subscripts

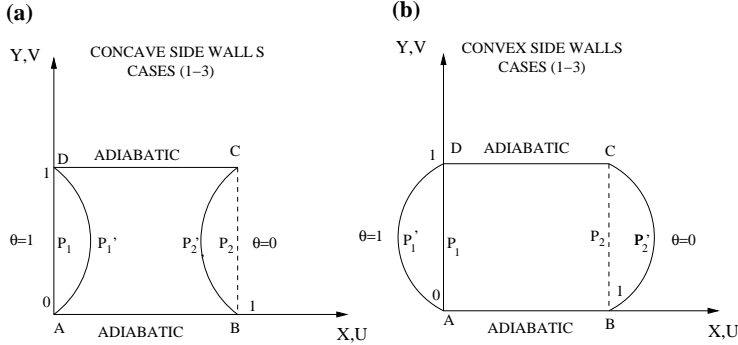| k | node number |
| l | left wall |
| r | right wall |

Figure 1: Schematic diagram of the computational domain for enclosure with (a) concave and (b) convex side walls.

MATHEMATICAL MODELLING AND SIMULATIONS

The computational domain is shown in Figure 1(a-b) based on semi-infinite approximation along Z direction. Thermophysical properties of the fluid in the flow field are assumed to be constant except density. The variation of density with temperature can be calculated using Boussinesq approximation. In this way, the temperature field and flow fields are coupled. Under these assumptions, governing equations for steady two-dimensional natural convection flow in the square enclosure with curved side walls using conservation of mass, momentum and energy can be written with fol-

Table 1: Values of P_1P_1', a, b, c for left wall and P_2P_2', a', b', c' for right wall for all (a) concave and (b) convex cases.

(a)

	Concave								
	P_1P_1'	P_2P_2'	a	b	c	a'	b'	c'	S_{max}
Case 1	0.1	-0.1	-0.4	0.4	0	0.4	-0.4	1	1.026
Case 2	0.2	-0.2	-0.8	0.8	0	0.8	-0.8	1	1.098
Case 3	0.4	-0.4	-1.6	1.6	0	1.6	-1.6	1	1.333

(b)

	Convex								
	P_1P_1'	P_2P_2'	a	b	c	a'	b'	c'	S_{max}
Case 1	-0.1	0.1	0.4	-0.4	0	-0.4	0.4	1	1.026
Case 2	-0.2	0.2	0.8	-0.8	0	-0.8	0.8	1	1.098
Case 3	-0.4	0.4	1.6	-1.6	0	-1.6	1.6	1	1.333

lowing dimensionless variables or numbers:

$$X = \frac{x}{L}, \quad Y = \frac{y}{L}, \quad U = \frac{uL}{\alpha}, \quad V = \frac{vL}{\alpha}, \quad \theta = \frac{T - T_c}{T_h - T_c}$$

$$P = \frac{pL^2}{\rho\alpha^2}, \quad Pr = \frac{\nu}{\alpha}, \quad Ra = \frac{g\beta(T_h - T_c)L^3Pr}{\nu^2}$$

The governing equations in dimensionless forms for continuity [Eq. (1)], momentum balance [Eq. (2) and (3)] and energy balance [Eq. (4)] are as follows:

$$\frac{\partial U}{\partial X} + \frac{\partial V}{\partial Y} = 0, \tag{1}$$

$$U\frac{\partial U}{\partial X} + V\frac{\partial U}{\partial Y} = -\frac{\partial P}{\partial X} + Pr\left(\frac{\partial^2 U}{\partial X^2} + \frac{\partial^2 U}{\partial Y^2}\right), \tag{2}$$

$$U\frac{\partial V}{\partial X} + V\frac{\partial V}{\partial Y} = -\frac{\partial P}{\partial Y} + Pr\left(\frac{\partial^2 V}{\partial X^2} + \frac{\partial^2 V}{\partial Y^2}\right) + RaPr\theta, \tag{3}$$

$$U\frac{\partial \theta}{\partial X} + V\frac{\partial \theta}{\partial Y} = \frac{\partial^2 \theta}{\partial X^2} + \frac{\partial^2 \theta}{\partial Y^2} \tag{4}$$

and the governing equations [Eqs. (2)-(4)] are subjected to the following boundary conditions;

$$U = V = 0, \quad \frac{\partial \theta}{\partial Y}(X, 0) = 0, \text{ for } Y = 0 \qquad \text{on wall AB}$$

$$U = V = 0, \quad \theta = 0, \text{ for } X = aY^2 + bY + c \quad \text{on wall BC}$$

$$U = V = 0, \quad \frac{\partial \theta}{\partial Y}(X, 1) = 0, \text{ for } Y = 1 \qquad \text{on wall CD}$$

$$U = V = 0, \quad \theta = 1, \text{ for } X = a'Y^2 + b'Y + c' \quad \text{on wall DA} \tag{5}$$

Note that, a, b, c, a', b' and c' are dimensionless numbers. The coefficients of the quadratic equation are calculated by Cramer's Rule using three coordinates for various convex and concave curves. The values of the dimensionless numbers for all the considered cases are given in Table 1(a-b).

The momentum and energy balance equations (Eqs. 2-4) are solved using the Galerkin finite element method. The continuity equation [Eq. (1)] has been used as

a constraint due to mass conservation and this constraint may be used to obtain the pressure distribution. In order to solve Eqs. (2)-(3), we use the penalty finite element method where the pressure, P is eliminated by a penalty parameter, γ and the incompressibility criteria given by [Eq. (1)] which results in

$$P = -\gamma \left(\frac{\partial U}{\partial X} + \frac{\partial V}{\partial Y} \right) \tag{6}$$

The continuity equation [Eq. (1)] is automatically satisfied for large values of γ. Typical values of γ that yield consistent solutions are 10^7. Using Eq. (6), the momentum balance equations [Eqs. (2) and (3)] reduce to

$$
\begin{aligned}
U \frac{\partial U}{\partial X} + V \frac{\partial U}{\partial Y} &= \gamma \frac{\partial}{\partial X} \left(\frac{\partial U}{\partial X} + \frac{\partial V}{\partial Y} \right) \\
&+ Pr \left(\frac{\partial^2 U}{\partial X^2} + \frac{\partial^2 U}{\partial Y^2} \right)
\end{aligned} \tag{7}
$$

and

$$
\begin{aligned}
U \frac{\partial V}{\partial X} + V \frac{\partial V}{\partial Y} &= \gamma \frac{\partial}{\partial Y} \left(\frac{\partial U}{\partial X} + \frac{\partial V}{\partial Y} \right) \\
&+ Pr \left(\frac{\partial^2 V}{\partial X^2} + \frac{\partial^2 V}{\partial Y^2} \right) + Ra\, Pr\, \theta
\end{aligned} \tag{8}
$$

The system of equations [Eqs. (4), (7) and (8)] with boundary conditions [Eq. (5)] are solved using the Galerkin finite element method [11]. Expanding the velocity components (U, V) and temperature (θ) using basis set $\{\Phi_k\}_{k=1}^N$ as,

$$U \approx \sum_{k=1}^N U_k\, \Phi_k(X,Y)\,, \quad V \approx \sum_{k=1}^N V_k\, \Phi_k(X,Y) \quad \text{and}$$

$$\theta \approx \sum_{k=1}^N \theta_k\, \Phi_k(X,Y) \tag{9}$$

The Galerkin finite element method yields nonlinear residual equations for Eqs. (4), (7) and (8) at nodes of internal domain Ω. The detailed solution procedure is given in an earlier work [4].

Streamfunction
The fluid motion is displayed using the streamfunction (ψ) obtained from velocity components U and V. The relationships between streamfunction, (ψ) and velocity components for two dimensional flows are

$$U = \frac{\partial \psi}{\partial Y}\,, \quad V = -\frac{\partial \psi}{\partial X} \tag{10}$$

which yield a single equation

$$\frac{\partial^2 \psi}{\partial X^2} + \frac{\partial^2 \psi}{\partial Y^2} = \frac{\partial U}{\partial Y} - \frac{\partial V}{\partial X} \tag{11}$$

Using the above definition of the streamfunction, the positive sign of ψ denotes anticlockwise circulation and the clockwise circulation is represented by the negative sign of ψ. The no-slip condition is valid at all boundaries as there is no cross flow, hence $\psi = 0$ is used as residual equations at the nodes for the boundaries. The bi-quadratic basis function is used to evaluate the integrals in the residual equation and ψ's are obtained by solving the N linear residual equations and the detailed solution procedure are reported in an earlier work [4].

Nusselt number
The heat transfer coefficient in terms of the local Nusselt number (Nu) is defined as

$$Nu = -\frac{\partial \theta}{\partial n} \tag{12}$$

where n denotes the normal direction on a plane. The normal derivative is evaluated using the bi-quadratic basis set. The local Nusselt numbers at left wall (Nu_l) and right wall (Nu_r) are defined as

$$Nu_l = \sum_{i=1}^9 \theta_i \left(\sin\varphi\, \frac{\partial \Phi_i}{\partial X} - \cos\varphi\, \frac{\partial \Phi_i}{\partial Y} \right) \tag{13}$$

$$Nu_r = \sum_{i=1}^9 \theta_i \left(-\sin\varphi\, \frac{\partial \Phi_i}{\partial X} + \cos\varphi\, \frac{\partial \Phi_i}{\partial Y} \right) \tag{14}$$

The average Nusselt numbers at the side walls are

$$\overline{Nu_l} = \frac{\int_0^S Nu_l\, ds'}{\int_0^S ds'} \quad \text{and} \quad \overline{Nu_r} = \frac{\int_0^S Nu_r\, ds'}{\int_0^S ds'} \tag{15}$$

Here S is the length and ds' is the small elemental length along the curved wall.

Heatfunction
The heat flow within the enclosure is displayed using the heatfunction (Π) obtained from conductive heat fluxes ($-\frac{\partial \theta}{\partial X}$, $-\frac{\partial \theta}{\partial Y}$) as well as convective heat fluxes ($U\theta$, $V\theta$). The heatfunction satisfies the steady energy balance equation [Eq. (4)] [1] such that

$$
\begin{aligned}
\frac{\partial \Pi}{\partial Y} &= U\theta - \frac{\partial \theta}{\partial X} \\
-\frac{\partial \Pi}{\partial X} &= V\theta - \frac{\partial \theta}{\partial Y}
\end{aligned} \tag{16}
$$

which yield a single equation

$$\frac{\partial^2 \Pi}{\partial X^2} + \frac{\partial^2 \Pi}{\partial Y^2} = \frac{\partial}{\partial Y}(U\theta) - \frac{\partial}{\partial X}(V\theta) \tag{17}$$

The residual equation is further supplemented with various Dirichlet and Neumann boundary conditions in order to obtain an unique solution. Neumann boundary conditions of Π are obtained for isothermal (hot or cold) walls as derived from Eq. (16) and are specified as $\mathbf{n} \cdot \nabla \Pi = 0$ for isothermal hot left wall or isothermal cold tight wall.

The top and bottom insulated walls may be represented by Dirichlet boundary condition as obtained from Eq. (16) which is simplified into $\frac{\partial \Pi}{\partial X} = 0$ for an adiabatic wall. A reference value of Π is assumed as 0 at $X = 0, Y = 0$ and hence $\Pi = 0$ is valid for $Y = 0, \forall X$. The value of Π at the top wall is obtained as, $\Pi = S_{max}\overline{Nu_l}$ for $Y = 1, \forall X$. Note that, S_{max} is length of the curved wall. It may be noted that, the unique solution of Eq. (17) is strongly dependent on the non-homogeneous Dirichlet conditions. At the top horizontal wall BC, boundary condition for Π may be obtained by integrating Eq. (16).

$$
\begin{aligned}
\Pi(0,1) &= \Pi(0,0) + \int_0^{S_{max}} \left(\frac{\partial \Pi}{\partial s'} \right) ds' \\
&= \Pi(0,0) + S_{max}\overline{Nu_l} \\
&= S_{max}\overline{Nu_l} = \Pi(1,1) = \Pi(X,1)
\end{aligned} \tag{18}
$$

Entropy generation

During natural convection, entropy generation occurs due to heat transfer irreversibility and fluid friction irreversibility. Considering a control volume which allows both mass and energy transport with the surrounding and assuming local thermodynamic equilibrium, the total local entropy generation for a two-dimensional natural convection system [7] in Cartesian coordinates may be written as follows:

$$
\begin{aligned}
\dot{S}'''_{gen} =\ & \frac{k}{T_0{}^2}\left[\left(\frac{\partial T}{\partial x}\right)^2 + \left(\frac{\partial T}{\partial y}\right)^2\right] \\
& + \frac{\mu}{T_0}\left[2\left(\left(\frac{\partial u}{\partial x}\right)^2 + \left(\frac{\partial v}{\partial y}\right)^2\right) + \left(\frac{\partial v}{\partial x} + \frac{\partial u}{\partial y}\right)\right]
\end{aligned}
\tag{19}
$$

The first term [square bracketed] in Eq. 19 is the entropy generation due to heat transfer caused by temperature gradient and second term [square bracketed] represents the entropy generation due to fluid friction caused by velocity gradient. As seen from Eq. 19, the entropy generation rate is positive and finite as long as temperature and velocity gradients are present in the system. Also, the entropy generation due to fluid friction and heat transfer are strongly interrelated with geometric characteristics the system. The dimensionless form of Eq. 19 based on individual terms of entropy generation due to heat transfer (S_θ) and entropy generation due to fluid friction (S_ψ) may be written as follows:

$$
S_\theta = \left[\left(\frac{\partial \theta}{\partial X}\right)^2 + \left(\frac{\partial \theta}{\partial Y}\right)^2\right]
\tag{20}
$$

$$
S_\psi = \phi\left\{2\left[\left(\frac{\partial U}{\partial X}\right)^2 + \left(\frac{\partial V}{\partial Y}\right)^2\right] + \left(\frac{\partial U}{\partial Y} + \frac{\partial V}{\partial X}\right)^2\right\}
\tag{21}
$$

In above equation, ϕ is called irreversibility distribution ratio, defined as:

$$
\phi = \frac{\mu T_o}{k}\left(\frac{\alpha}{L\Delta T}\right)^2
\tag{22}
$$

In the current study, ϕ is taken as 10^{-4}. A similar value for ϕ was considered by Ilis et al. [8]. After calculating the velocity components and temperature field, the known temperature and velocity fields are incorporated in the derivative terms of the expression for entropy generation. As mentioned earlier, the derivatives are evaluated based on finite element method. Nine node bi-quadratic elements are used with each element mapped using iso-parametric mapping [4] from $X-Y$ to a unit square $\xi-\eta$ domain. The domain integrals in the residual are evaluated using nine node bi-quadratic basis functions in $\xi-\eta$ domain. The derivative of any function f over an element e is written as:

$$
\frac{\partial f^e}{\partial n} = \sum_{k=1}^{9} f_k^e \frac{\partial \Phi_k^e}{\partial n}
\tag{23}
$$

where, f_k^e is the value of the function at local node k in the element e and Φ_k^e is the value of basis function at local node k in the element e. Further, since each node is shared by four elements (in the interior domain) or two elements (along the boundary), the value of the derivative of any function at the global node number (i), is averaged over those shared elements (N^e), i.e.,

Table 2: Comparisons of present results with benchmark solution [12, 13] for natural convection in square cavity in presence of air ($Pr = 0.71$), at various Ra.

Ra	Present work		Deng and Tang [12]		Wan et. al. [13]	
	$\lvert\psi\rvert_{max}$	$\overline{Nu}$	$\lvert\psi\rvert_{max}$	$\overline{Nu}$	$\lvert\psi\rvert_{max}$	$\overline{Nu}$
10^3	1.17	1.118	1.17	1.118	-	1.117
10^4	5.07	2.248	5.04	2.254	-	2.254
10^5	9.61	4.564	9.50	4.557	-	4.598

$$
\frac{\partial f_i}{\partial n} = \frac{1}{N^e}\sum_{e=1}^{N^e}\frac{\partial f_i^e}{\partial n}
\tag{24}
$$

Therefore, at each node, local entropy generation for thermal ($S_{\theta,i}$) and fluid friction ($S_{\psi,i}$) are given by,

$$
S_{\theta,i} = \left[\left(\frac{\partial \theta_i}{\partial X}\right)^2 + \left(\frac{\partial \theta_i}{\partial Y}\right)^2\right]
\tag{25}
$$

$$
S_{\psi,i} = \phi\left\{2\left[\left(\frac{\partial U_i}{\partial X}\right)^2 + \left(\frac{\partial V_i}{\partial Y}\right)^2\right] + \left(\frac{\partial U_i}{\partial Y} + \frac{\partial V_i}{\partial X}\right)^2\right\}
\tag{26}
$$

Note that, the derivatives, $\frac{\partial \theta_i}{\partial X}, \frac{\partial \theta_i}{\partial Y}, \frac{\partial U_i}{\partial X}, \frac{\partial U_i}{\partial Y}, \frac{\partial V_i}{\partial X}, \frac{\partial V_i}{\partial Y}$ are evaluated following Eq. 24. The combined total entropy generation (S_{total}) in the cavity is given by the summation of total entropy generation due to heat transfer ($S_{\theta,total}$) and fluid friction ($S_{\psi,total}$), which in turn are obtained via integrating the local entropy generation rates ($S_{\theta,i}$ and $S_{\psi,i}$) over the domain Ω.

$$
S_{total} = S_{\theta,total} + S_{\psi,total}
\tag{27}
$$

where,

$$
S_{\theta,total} = \int_\Omega \left\{\left[\frac{\partial}{\partial X}\left(\sum_{k=1}^N \theta_k\Phi_k\right)\right]^2 + \left[\frac{\partial}{\partial Y}\left(\sum_{k=1}^N \theta_k\Phi_k\right)\right]^2\right\} dXdY
\tag{28}
$$

$$
\begin{aligned}
S_{\psi,total} =\ & \phi\int_\Omega\left\{2\left[\frac{\partial}{\partial X}\left(\sum_{k=1}^N U_k\Phi_k\right)\right]^2 + 2\left[\frac{\partial}{\partial Y}\left(\sum_{k=1}^N V_k\Phi_k\right)\right]^2\right. \\
& \left. + \left[\frac{\partial}{\partial Y}\left(\sum_{k=1}^N U_k\Phi_k\right) + \frac{\partial}{\partial X}\left(\sum_{k=1}^N V_k\Phi_k\right)\right]^2\right\} dXdY
\end{aligned}
\tag{29}
$$

The integrals are evaluated using three-point element-wise Gaussian quadrature integration method. The relative dominance of entropy generation due to heat transfer and fluid friction is given by Bejan number (Be_{av}), a dimensionless parameter defined as

$$
Be_{av} = \frac{S_{\theta,total}}{S_{\theta,total} + S_{\psi,total}} = \frac{S_{\theta,total}}{S_{total}}
\tag{30}
$$

Therefore, $Be_{av}>0.5$ implies dominance of heat transfer irreversibility and $Be_{av}<0.5$ implies dominance of fluid friction irreversibility.

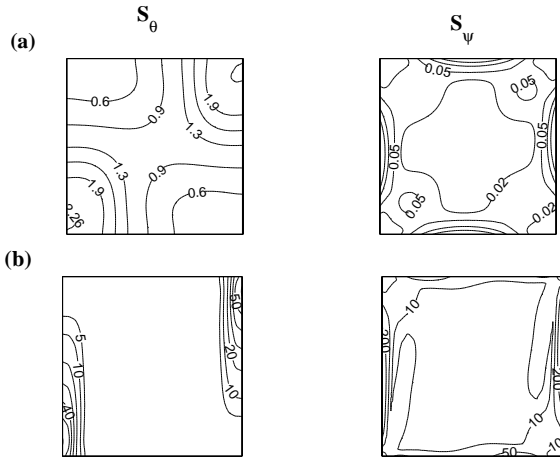Figure 2: Local entropy generation due to heat transfer S_θ and fluid friction S_ψ for a square enclosure with hot left wall, cold right wall and adiabatic horizontal walls as reported by Ilis et. al. [8] for $Pr = 0.71$, (a) $Ra = 10^3$ and (b) $Ra = 10^5$.

RESULTS AND DISCUSSION

Numerical tests and parameters

The computational domain in $\xi - \eta$ coordinate system consists of 28×28 bi-quadratic elements which correspond to 57×57 grid points. The computational grid with curved side walls is generated by mapping the curved domain into a regular square domain in $\xi - \eta$ coordinate system [4]. The bi-quadratic elements with a lesser number of nodes smoothly capture the nonlinear variations of the field variables, which are in contrast with finite-difference/finite-volume solutions. In the current investigation, Gaussian quadrature based finite element method provides smooth solutions at the interior domain including the corner regions as evaluation of residuals depends on interior Gauss points and thus the effect of corner nodes is less pronounced in the final solution. Benchmark studies were carried out for the square cavity with a hot left wall and a cold right wall in presence of adiabatic horizontal walls, similar to the case reported by Deng and Tang [12] and Wan et. al. [13]. Results are compared in terms of average Nusselt number $(\overline{Nu_r})$ and maximum streamfunction $(|\psi|_{max})$ value for a square enclosure as reported by Deng and Tang [12] for various Ra [see Table 2]. The results in terms of average Nusselt number as reported by Wan et al. [13] are compared with the current work [see Table 2] and the results are in good agreement with earlier works [12, 13]. Benchmark studies are also carried out in terms of S_θ and S_ψ for a differentially heated square enclosure at $Pr = 0.71$ and $Ra = 10^3 - 10^5$ as reported by Ilis et. al. [8]. The results in terms of S_θ and S_ψ [see Figure 2] are in very good agreement with the previous work [8].

Three cases based on three different curvatures of the concave side walls are considered. The original square enclosure is modified to a curved walled enclosure by shifting the mid points of the side walls, P_1 and P_2 in the inward direction to P_1' and P_2', respectively, such that $AP_1'D$ and $BP_2'C$ form curves which obey the quadratic equations; $X = aY^2 + bY + c$ and $X = a'Y^2 + b'Y + c'$, respectively [see Figure 1(a) and Table 1(a)]. The values of P_1P_1' or
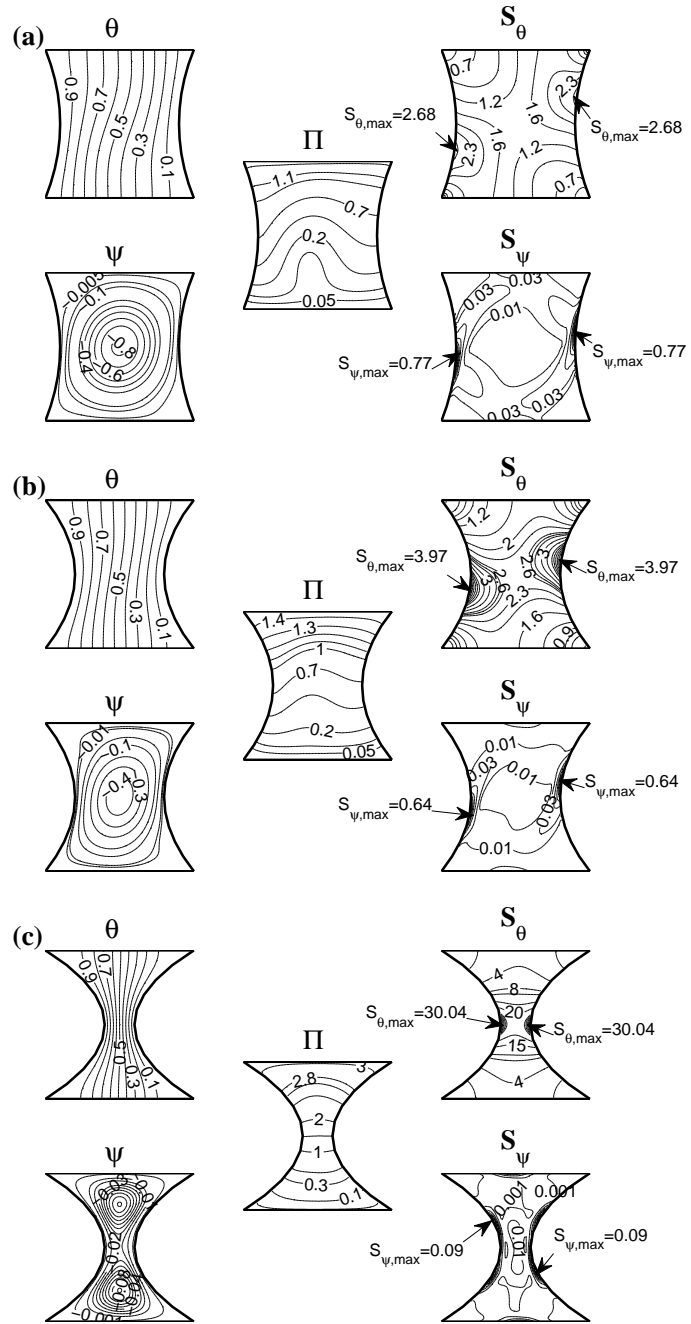

Figure 3: Isotherms (θ), entropy generation due to heat transfer (S_θ) heatlines (Π), streamlines (ψ) and entropy generation due to fluid friction (S_ψ) at $Pr = 0.01$ and $Ra = 10^3$ for all concave cases: (a) case 1, (b) case 2 and (c) case 3.

P_2P_2' are assumed to be $L/10, 2L/10$ and $4L/10$ for case 1, case 2 and case 3, respectively, where L is the height or length of base of the cavity.

Figure 3(a-c) illustrate isotherms (θ), streamlines (ψ), entropy generation maps (S_θ and S_ψ) and heatlines (Π) for concave cases (cases 1-3) at low Ra ($Ra = 10^3$) and $Pr = 0.01$. The isotherms are smooth vertical lines perpendicular to the adiabatic horizontal walls indicating conduction dominant heat transfer for all cases at low Ra. The boundary layer thickness gradually becomes larger at the corner regions of the enclosure as the wall curvature increases from case 1 to case 3. Thus, heat distribution is inadequate in the corner regions of the enclosure in case 3

as seen from the presence of hot stagnant fluid at the left corner regions and cold stagnant fluid at the right corner regions. Conductive heat transfer is intense at the throat region in case 3 and that can also be explained based on compressed isotherms near the middle portion of the enclosure. It is found that S_θ is observed to be negligible at the corner region of the enclosure, especially in case 3 due to very less heat transfer rate at those region. Also, S_θ is maximum near the middle portion of the side walls for all the cases. Largest value of S_θ in case 3 is attributed to very high conductive heat transfer at the middle portion of side walls based on compressed isotherms. At the interior locations of the enclosure, except the corner regions local S_θ is found to be significant in case 3, compared to cases 1 and 2. Thus, overall entropy generation due to heat transfer (S_θ) is larger in case 3 throughout the enclosure, especially at the core compared to that of cases 1 and 2. At lower Ra and Pr, single and smooth fluid circulation cells span the entire enclosure for cases 1 and 2 [Figure 3(a-b)]. Due to the imposed thermal boundary condition, fluid from the lower part of the left wall gets heated up and moves upward due to buoyancy force and flows down along the cold right wall. Fluid circulation cell gets segregated at the core and two clockwise rotating loops are observed in case 3 due to the effect of highly concave side walls. Strength of fluid circulation cell is highest in case 1 and least in case 3. As the flow circulation cells are weaker at low Ra, entropy generation due to flow irreversibilities (S_ψ) is also smaller for all cases. Velocity gradient between the rotating fluid and solid wall is very high near the stagnant walls, thus, S_ψ is significant near the solid walls for all cases. At the core, velocity gradient between the rotating fluid layers is quite less and the entropy generation due to fluid friction is negligible near the central regime compared to that of solid walls for all cases. It may be noted that, $S_{\psi,max}$ is highest for case 1 compared to cases 2 and 3. Due to larger available area for fluid circulation for case 1 which in turn results in comparatively high magnitude of streamfunction which further leads to larger velocity gradient at the solid walls. In contrast, due to highly curved side walls, the available area for fluid flow is very less and $|\psi|$ is less for case 3, that leads to lesser velocity gradients. Note that, $S_{\psi,max} = 0.77, 0.64$ and 0.09 for case 1, case 2 and case 3, respectively.

The direction and magnitude of heat flow in the enclosure can be demonstrated via heatlines and heatfunctions, respectively [see Figure 3(a-c)]. As the intensity of fluid flow is less at low Ra, end-to-end heatlines connecting two side walls are observed in the cavity. Slightly distorted heatlines are observed in the core region for case 1 and case 2 due to comparatively stronger convective effect in those cases. Heatlines are smooth and almost straight lines at core in case 3 depicting highly conductive heat transfer. Overall, the heat transfer in the cavity is conduction dominant in all the cases and highest heat transfer rate is observed in case 3. This can also be explained from the heatline contours where dense end-to-end heatlines are observed in the central portion of the enclosure in case 3.

At high Ra, isotherms at the core are highly distorted and compressed along bottom portion of the left wall and top portion of the right wall especially in cases 1 and 2, signifying dominance of convection as seen from
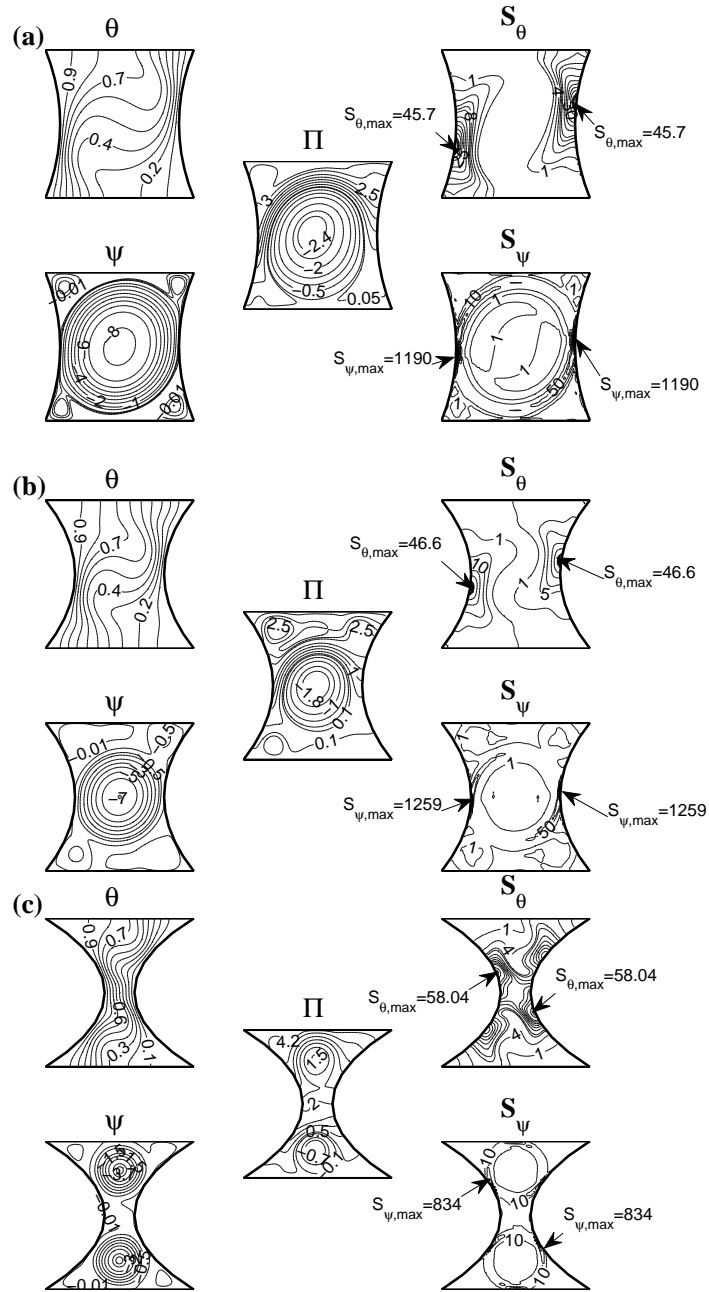

Figure 4: Isotherms (θ), entropy generation due to heat transfer (S_θ) heatlines (Π), streamlines (ψ) and entropy generation due to fluid friction (S_ψ) at $Pr = 0.01$ and $Ra = 10^5$ for all concave cases: (a) case 1, (b) case 2 and (c) case 3.

Figure 4(a-c). The thicknesses of thermal boundary layer at the bottom portion of left wall and top portion of right wall are observed to be lesser compared to that of low Ra cases [see Figure 3 and 4]. Isotherms are observed to be highly compressed towards the entire left and right walls, except the top left and bottom right corners for case 3. As a result of highly concave walls, compression of isotherms along the left and right walls are more pronounced for case 3 compared to that of cases 1 and 2. As a consequence, larger thermal gradient in case 3 results in higher S_θ for case 3. Note that, $S_{\theta,max}$ is almost identical for cases 1 and 2, as there is no significant variation in thermal gradients. Note that, $S_{\theta,max} = 45.7$ and 46.6 occur for cases 1 and 2, respectively. Zones of $S_{\theta,max}$ are found near the

lower portion of left wall and upper portion of right wall for case 1, whereas for case 2, $S_{\theta,max}$ occurs almost at the middle portions of side walls. In contrast, $S_{\theta,max}$ is observed at the top portion of the left wall and bottom portion of the right walls with $S_{\theta,max} = 58.04$ for case 3. Due to significant temperature uniformity based on intense convection for case 1, thermal gradients are less and thus, S_θ is less at the interior region. At the core, local S_θ is slightly larger for case 2 than that of case 1 due to comparatively higher temperature gradient for case 2. It is interesting to note that, S_θ is significantly larger at the interior region for case 3 due to very high thermal gradient at the throat region. Note that, boundary layer thickness is larger at the corner regions and S_θ is negligible at the corner regions in all cases and this effect is more prominently visible in case 3. Enhanced buoyancy force results in stronger fluid circulation cells as seen from the magnitude of streamfunctions for all cases at $Ra = 10^5$ [see Figure 4(a-c)]. In addition to primary fluid circulation cell, multiple fluid circulation cells are also observed near the corner regions of the enclosure especially in cases 1 and 2. Larger velocity gradient exists near the side walls due to larger velocity gradients at high Ra compared to that of low Ra cases. Thus, S_ψ is comparatively higher for all cases compared to low Ra cases. It may be noted that, $S_{\psi,max}$ for cases 1 and 2 are observed at the middle portions of curved side walls due to larger velocity gradients at those zones. The complex fluid flow pattern in case 3 results in higher velocity gradient near the top and bottom portions of the side walls. Consequently, $S_{\psi,max}$ for case 3 is observed near the top portion of left wall and bottom portion of right wall. Comparative study of all cases shows that due to higher velocity gradient at the side walls in case 2, $S_{\psi,max}$ is highest in case 2 followed by case 1 and case 3. It may be noted that, $S_{\psi,max} = 1190, 1259$ and 834 for cases 1, 2 and 3, respectively. Active zones of S_ψ also occur at the middle portions of the horizontal walls for all cases. One circular pattern in the S_ψ contours are observed at the core for cases 1 and 2. Due to effect of segregated streamline cells at the top and bottom halves, two circular patterns of S_ψ are observed at the top and bottom halves of the enclosure in case 3. At the interior zone, velocity gradient is larger for case 3 than that of cases 1 and 2 which can also be explained based on the magnitude of S_ψ.

In contrast to low Ra, intense closed loop heatline cells are seen at the core of the cavity for cases 1 and 2, whereas the circulation cells are segregated and two heatline cells are seen at the top and bottom halves of the cavity for case 3 [see Figure 4(a-c)]. As a result of high thermal mixing in case 1, convective heat transfer rate is highest in case 1. Denser heatlines at the middle portion of left wall signify large amount of heat being drawn from the middle portion of the wall for all cases. Sparse heatlines are observed near the lower right corner of the cavity depicting very less amount of heat being delivered to those regions for all cases. In addition, very small secondary heat circulation cells are observed at the corner regions of the cavity for all cases. Note that, central portion of the cavity is filled with closed loop heatlines for case 1 and 2, whereas dense end-to-end heatlines are observed in the central portion (throat region) for case 3. Heatlines are denser at the middle portion of left and right walls depicting high heat transfer at those regions for cases 1 and 2. On the other hand, sparse

end-to-end heatlines are seen at the middle portion of the cavity for case 3. Also, it may be noted that, dense heatlines are found at the top and bottom portion of the left wall for case 3.
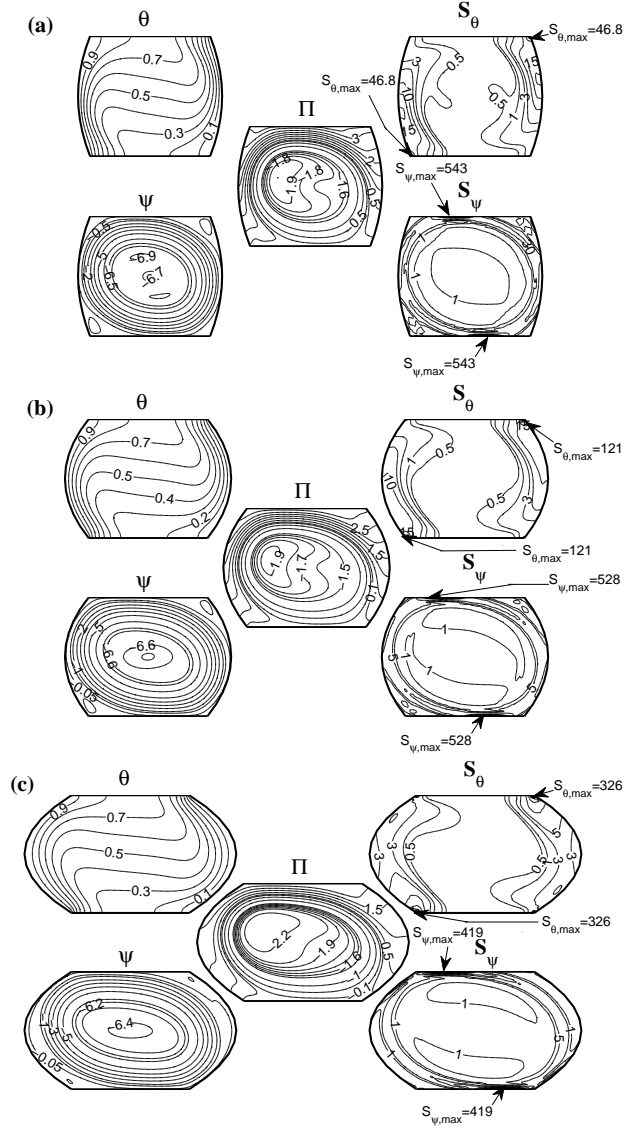

Figure 5: Isotherms (θ), entropy generation due to heat transfer (S_θ) heatlines (Π), streamlines (ψ) and entropy generation due to fluid friction (S_ψ) at $Pr = 0.01$ and $Ra = 10^5$ for all convex cases: (a) case 1, (b) case 2 and (c) case 3.

The enclosure with convex side walls is considered with three cases based on three different curvatures of side walls. Similar to the concave case, the square enclosure is modified to a curved walled enclosure by shifting the point P_1 and P_2 to P_1' and P_2', respectively in the outward direction such that $AP_1'D$ and $BP_2'C$ form curves which obey the quadratic equations; $X = aY^2 + bY + c$ and $X = a'Y^2 + b'Y + c'$, respectively [see Figure 1(b) and Table 1(b)]. The values of P_1P_1' or P_2P_2' are same as in the concave case which are $L/10, 2L/10$ and $4L/10$ for case 1, case 2 and case 3, respectively.

Figure 5(a-c) display isotherms, streamlines and entropy generation maps due to heat transfer and fluid friction (S_θ and S_ψ) and heatlines (Π) at $Ra = 10^5$ and $Pr = 0.01$ for all convex cases. Due to large convective effect at high Ra, thermal mixing is significant at the core

for all cases. Consequently, isotherms are highly distorted at the core and compressed towards the entire left and right walls. Note that, the strength of compression of isotherms are high for convex cases compared to that of concave cases [see Figure 4 and 5] As a result, S_θ is significantly large throughout the left and right walls in all cases. Larger compression of isotherms towards the top right and bottom left corner results in larger thermal gradient which further results in maximum S_θ at those regions for all convex cases. As wall curvature increases from case 1 to case 3, heat transfer irreversibility at the top right corner and bottom left corner increases, which is similar to concave cases. Note that, $S_{\theta,max} = 46.8$, 121 and 326 occur for cases 1, 2 and 3, respectively. It may be noted that, thermal gradients are larger for convex cases due to higher convective effect and that results in larger $S_{\theta,max}$ for convex cases compared to that of concave cases. At the core of the cavity, local S_θ is observed to be almost similar for all convex cases with $S_\theta \approx 0.5$. Due to high thermal mixing for convex cases, isotherms are distorted and temperature gradient is less and thus, S_θ is lesser for convex cases than that of concave cases at the core [see Figure 4 and 5]. Active zones for S_θ are also observed at the corner regions for all convex cases which is in contrast to concave cases, where S_θ was very less at the corner zones. At $Ra = 10^5$, the fluid flow intensity is high and that results in enhanced convective transport inside the cavity for all cases [see Figure 5]. Due to large thermal diffusivity, tiny secondary fluid circulation cells are observed at the top right and bottom left corner of the cavity for all cases. Maximum entropy generation due to fluid friction is largest in case 1 ($S_{\psi,max} = 543$) compared to that of case 2 ($S_{\psi,max} = 528$) and case 3 ($S_{\psi,max} = 419$), which occur near the left portions of top wall and right portion of bottom wall for all cases, which is in contrast to concave cases. Velocity gradients at the core decrease with increase in wall curvature from case 1 to case 3 and S_ψ at the core is least for case 3.

As Ra increases to 10^5, many interesting features are observed in the trends of heatlines [see Figure 5]. Highly intense closed loop heatline cells are found at the core and they are compressed towards the top left corner of the enclosure. Both end-to-end and closed loop heatlines are found in the enclosure, however, the magnitude of closed loop heatline circulation cells are significantly higher. Higher intensity of closed loop heatlines depict recirculation of heat energy due to enhanced thermal mixing in the core for all cases. Dense heatlines emanating from the left wall illustrate high convective heat transfer from the entire left wall to the entire right wall in all the cases. The convective heat transport is more dominant in convex case compared to that of convex cases [see Figure 4 and 5]. This can also be inferred from more intense heatline cells for convex cases compared to concave cases. Enhanced thermal mixing causes the heatlines to get pushed towards the bottom left corner and top right corner for all cases.

Average Nusselt number, total entropy generation and average Bejan number

The variations of total entropy generation due to heat transfer and fluid friction irreversibilities (S_{total}), average Bejan number (Be_{av}) and average Nusselt number on the curved right wall ($\overline{Nu_r}$) vs logarithmic Rayleigh number
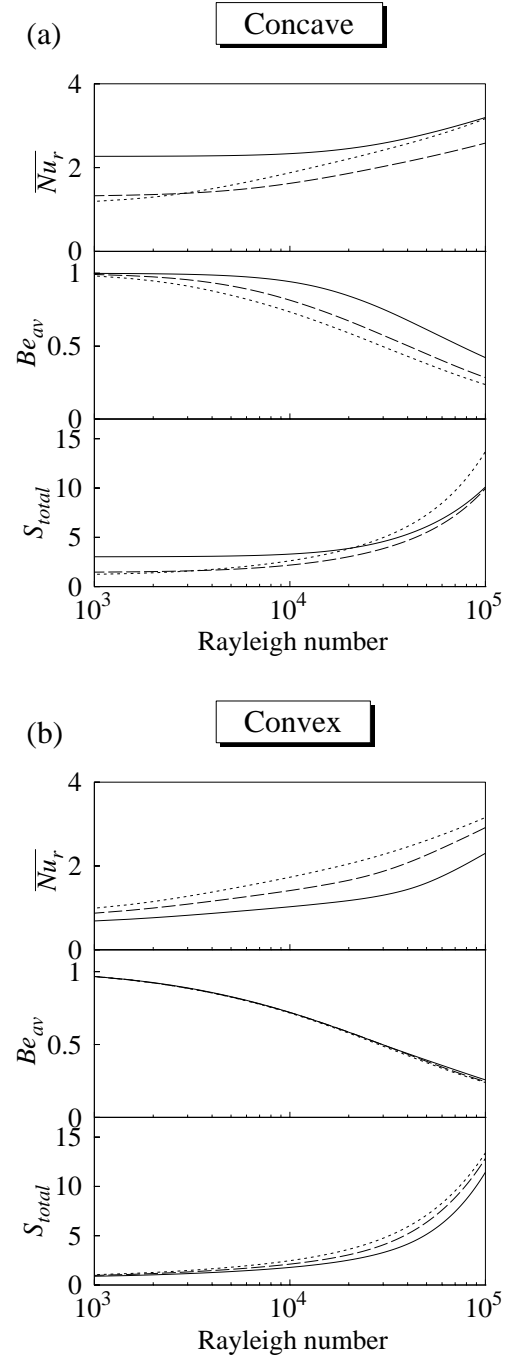

Figure 6: Variations of total entropy generation (S_{total}: bottom panel), average Bejan number (Be_{av}: middle panel), and average Nusselt number at the right wall (Nu_r: top panel) with Ra at $Pr = 0.01$ for (a) concave cases [case 1 (- - - - -), case 2 ($- - - -$) and case 3 (———)] and (b) convex cases [case 1 (- - - - -), case 2 ($- - - -$) and case 3 (———)].

(Ra) are presented in bottom, middle and top panels of Figure 6(a-b), respectively, for both concave and convex cases at $Pr = 0.01$.

Figure 6(a) represents distributions of S_{total}, Be_{av} and $\overline{Nu_r}$ for $Pr = 0.01$ for all concave cases. The total entropy generation (S_{total}) in the cavity increases slowly until $Ra \leq 10^4$ for all cases [see bottom panel of Figure 6(a)]. This is due to the fact that $S_{\psi,total}$ is very less compared to $S_{\theta,total}$ due to negligible convective effect and contribution of $S_{\psi,total}$ on S_{total} is negligible at low Ra. Note that, at

$Ra = 10^3$, $S_{\theta,total} = 1.22$ and $S_{\psi,total} = 0.02$ occur for case 1; $S_{\theta,total} = 1.45$ and $S_{\psi,total} = 0.01$ occur for case 2 and $S_{\theta,total} = 3.02$ and $S_{\psi,total} = 0.002$ occur for case 3. It may also be noted that, $S_{\theta,total} = 1.92$ and $S_{\psi,total} = 0.69$ occur for case 1; $S_{\theta,total} = 1.77$ and $S_{\psi,total} = 0.40$ occur for case 2 and $S_{\theta,total} = 3.10$ and $S_{\psi,total} = 0.19$ occur for case 3 at $Ra = 10^4$. As seen from the magnitudes of $S_{\theta,total}$ and $S_{\psi,total}$, it is observed that although $S_{\psi,total}$ is less for case 3, $S_{\theta,total}$ is significantly larger for case 3 compared to that of cases 1 and 2 at low Ra. As a result, larger S_{total} is observed for case 3 compared to all other cases at low Ra. Convection heat transfer is observed to be initiated at $Ra = 10^4$ all cases. Due to gradual increase of both fluid friction and heat transfer irreversibility at higher Ra, S_{total} increases rapidly for $Ra \geq 10^4$ for all cases. Note that, at $Ra = 10^5$, fluid flow irreversibility is larger and that can also be observed from the S_ψ contours of Figure 5. At $Ra = 10^5$, $S_{\theta,total} = 2.23$ and $S_{\psi,total} = 10.46$ occur for case 1; $S_{\theta,total} = 2.82$ and $S_{\psi,total} = 7.12$ occur for case 2 and $S_{\theta,total} = 4.25$ and $S_{\psi,total} = 5.84$ occur for case 3. As area available for fluid motion is larger for case 1 that results in larger fluid velocity. Hence, fluid flow irreversibility is significantly higher and thus, S_{total} is largest for case 1 at $Ra = 10^5$. In contrast to lower Ra, S_{total} is least for case 3 which is due to lesser $S_{\psi,total}$ at high Ra.

Distribution of average Bejan number (Be_{av}) indicates the dominance of entropy generation due to heat transfer or fluid friction during natural convection. Note that, $Be_{av} \geq 0.5$ indicates entropy generation is due to heat transfer and $Be_{av} \leq 0.5$ indicates entropy generation due to fluid friction. A generalized decreasing trend of Be_{av} with Ra may be observed for all cases [see the middle panel plots of Figure 6(a)]. At $Ra = 10^3$, $Be_{av} = 1$, which signifies that the entropy generation in the cavity is mainly due to heat transfer for all cases. As Ra increases further, Be_{av} decreases for cases 1 and 2 depicting dominance of fluid flow irreversibility over heat transfer irreversibility at high Ra. Due to larger magnitude of $S_{\psi,toal}$ over of $S_{\theta,total}$, Be_{av} is found to be 0.23 and 0.28 for case 1 and 2, respectively at $Ra = 10^5$. On the other hand, even at high Ra ($Ra = 10^5$), $S_{\theta,total}$ dominates over $S_{\psi,total}$ for case 3 as seen from value of Be_{av} ($Be_{av} = 0.43$).

It is observed that, $\overline{Nu_r}$ increases slowly for $Ra \leq 10^4$ for all cases due to smaller temperature gradient near the right wall [top panel of Figure 6(a)]. This is due to less fluid velocity at low Ra that results in lesser convective force throughout the cavity. This can also be depicted from the smooth isotherms along the right wall for all case [see Figure 3(a-c)]. Due to larger thermal gradients at the throat region of case 3, $S_{\theta,total}$ is larger for case 3 for low Ra. In addition, it is interesting to observe that $\overline{Nu_r}$ is also larger for case 3 for $Ra \leq 10^4$. This is due to the fact that overall heat transfer rate due to thermal gradients is sufficiently high even with loss of available energy due to thermal gradients ($S_{\theta,total}$) for case 3 at low Ra. At high Ra, convective effect is high and several zones of compressed isotherms are seen at the right wall for all cases [see Figure 4(a-c)]. Thus, total entropy generation due to heat transfer and fluid friction is larger than that of low Ra for all cases. It is interesting to note that, $S_{\theta,total}$ is high, but $\overline{Nu_r}$ is also high for all cases at high Ra. This is due to larger convective effect at high Ra that results in

stronger compression of isotherms at the right wall for all cases. It may be noted that, the loss of available energy in terms of $S_{\theta,total}$ is very less compared to that of the heat transfer due to temperature gradients. Largely compressed isotherms are seen at the top portion of right wall for case 1 and the top and middle portion of right wall for case 3. Thus, at $Ra = 10^5$, heat transfer rate due to thermal gradients are larger for cases 1 and 3 compared to that of case 2.

Figure 6(b) shows the distributions of S_{total}, Be_{av} and $\overline{Nu_r}$ with Ra at $Pr = 0.01$ for all convex cases. Similar to concave cases, S_{total} increases very slowly till $Ra = 10^4$ for all cases. This is due to conductive heat transfer in the cavity that results in negligible $S_{\psi,total}$ with larger and approximately constant $S_{\theta,total}$. At $Ra = 10^3$, $S_{\theta,total} = 1.01$ and $S_{\psi,total} = 0.03$ occur for case 1; $S_{\theta,total} = 0.93$ and $S_{\psi,total} = 0.03$ occur for case 2 and $S_{\theta,total} = 0.85$ and $S_{\psi,total} = 0.02$ occur for case 3. Note that, $S_{\theta,total} = 1.76$ and $S_{\psi,total} = 0.70$ occur for case 1; $S_{\theta,total} = 1.52$ and $S_{\psi,total} = 0.59$ occur for case 2 and $S_{\theta,total} = 1.28$ and $S_{\psi,total} = 0.49$ occur for case 3 for $Ra = 10^4$. Due to almost similar values of $S_{\theta,total}$ and $S_{\psi,total}$, the qualitative and quantitative trends of S_{total} are similar for all cases for $10^3 \leq Ra \leq 10^5$. As Ra increases further, S_{total} increases exponentially due to convection dominant heat transfer that results in rapid increase of both $S_{\psi,total}$ and $S_{\theta,total}$ for all cases. It may be noted that, $S_{\psi,total} = 10.19$, 9.69, 8.49 for cases 1, 2 ad 3, respectively at $Ra = 10^5$. Due to high convective force, the thermal gradients are also found to be high for all cases which can also be depicted from the magnitude of $S_{\theta,total}$ at high Ra. It may also be noted that, $S_{\theta,total} = 3.21$, 3.15, 2.94 for cases 1, 2 ad 3, respectively at $Ra = 10^5$. At high Ra, total entropy generation is largest for case 1, due to both high $S_{\theta,total}$ and $S_{\psi,total}$.

A steep decreasing trend of Be_{av} with Ra is observed for all convex cases case as seen from the middle panel of Figure 6(b). Note that, the qualitative as well as quantitative trends of Be_{av} are similar for all convex cases. Similar to concave cases, the maximum value for Be_{av} ($Be_{av} = 0.98$ for all cases) occurs at low $Ra = 10^3$, indicating that entropy generation in the cavity is primarily due to heat transfer irreversibility ($S_{\theta,total}$) at conduction dominant mode. As Ra increases to 10^5, fluid friction irreversibility ($S_{\psi,total}$) increases and that is significant compared to heat transfer irreversibility ($S_{\theta,total}$) due to enhanced convection heat transfer in the cavity. Thus, Be_{av} decreases with Ra for all cases as seen in the middle panel plot of Figure 6(b).

As Ra increases from 10^3 to 10^4, amount of heat transport to the right wall is found to be almost constant for all convex cases as seen from the top panel plot of Figure 6(b). At low Ra, smaller temperature gradient exists near the right wall which is due to weak fluid circulation cell that results in a low heat transport. This can also be illustrated from the smooth isotherms along the right wall for all convex cases at low Ra [figure not shown]. Slightly stronger compression of isotherms for case 1 results in larger thermal gradients at the top portion of the right wall for case 1 at low Ra. Thus, $S_{\theta,total}$ is slightly larger for case 1 compared to cases 2 and 3 for low Ra. In addition, overall heat transfer rate ($\overline{Nu_r}$) is also larger for

case 1 at low Ra ($Ra \leq 10^4$) as the temperature gradients is sufficiently high for case 1 although loss of available energy due to thermal gradients ($S_{\theta,total}$) is larger for case 1. As Ra increases ($Ra \geq 10^4$), due to enhanced convection, isotherms are highly compressed along the upper half of the right wall for all convex cases [see Figure 5(a-c)]. Thus, $S_{\theta,total}$ is higher at high Ra for all cases. The loss of available energy due to thermal gradients in terms of $S_{\theta,total}$ is less compared to that of the heat transfer due to temperature gradients at high Ra for all cases. As a result, overall heat transfer ($\overline{Nu_r}$) is higher for all cases at high Ra. Comparing all convex cases, largely compressed isotherms may be observed at the top half of right wall for case 1 at for all Ra. Thus, largest value of $\overline{Nu_r}$ is observed for case 1 eventhough considerable amount of energy is utilized to overcome significant heat transfer and fluid friction irreversibilities for all Ra.

CONCLUSION

In the present study, the analysis of heatlines and entropy generation due to heat transfer and fluid friction irreversibilities during natural convection within differentially heated cavities with concave/convex side walls has been performed. The flow and temperature distributions in addition to the entropy generation due to heat transfer and fluid friction are obtained for $Pr = 0.01$ and ($10^3 \leq Ra \leq 10^5$) for all cases. Direction and intensity of heat flow is also determined using heatlines concept. Further, analysis of average Nusselt number, total entropy generation and average Bejan number are carried out.

At low Ra ($Ra = 10^3$), heat transfer is primarily due to conduction based on less intense streamlines and smooth isotherms and heatlines for all cases. Enhanced convection is observed based on larger magnitudes of streamlines and closed loop heatlines in addition to distorted isotherms at $Ra = 10^5$ for all concave and convex cases. At low Ra, local entropy generation due to heat transfer and fluid friction are lower due to less velocity and temperature gradients for all cases. Due to enhanced convective effect higher Ra, streamline cells are stronger and isotherms are largely compressed that results in larger S_θ and S_ψ for all cases. Significant S_θ occurs near the middle portion of left and right walls for all concave cases at all Ra, whereas for convex cases, S_θ is significant at the top right and bottom left corners of the cavity. Also, $S_{\psi,max}$ is seen at the middle portion of the side walls for all concave cases while for convex cases, $S_{\psi,max}$ is seen at the middle portion of top and bottom walls.

At low Ra, $\overline{Nu_r}$ is largest for case 3 (concave) with moderate S_{total}. Largest $\overline{Nu_r}$ is observed for cases 1 and 3 for high Ra. It was also concluded that, S_{total} is largest for case 1 and lowest for case 3 at high Ra. Thus, throughout the range of Ra, case 3 may be chosen over cases 1 and 2 based on high $\overline{Nu_r}$ and less S_{total}. Based on moderate S_{total} and larger $\overline{Nu_r}$, case 1 (convex) may be energy efficient for all Ra.

REFERENCES

[1] Kimura S., Bejan A., The heatline visualization of convective heat transfer. *J. Heat Trans.-T. ASME* Vol. 105, 1983, pp. 916-919.

[2] Costa V. A. F., Bejan's heatlines and masslines for convection visualization and analysis, *Appl. Mech. Rev.* Vol. 59, 2006, pp. 126-145.

[3] Dalal A., Das M. K., Heatline method for the visualization of natural convection in a complicated cavity. *Int. J. Heat Mass Tran.* Vol. 51, 2008 pp. 263-272.

[4] Basak T., Roy S., Role of Bejans heatlines in heat flow visualization and optimal thermal mixing for differentially heated square enclosures. *Int. J. Heat Mass Tran.* Vol. 51, 2008, pp. 3486-3503.

[5] Anandalakshmi R., Basak T., Heat flow visualization analysis on natural convection in rhombic enclosures with isothermal hot side or bottom wall. *Europian J. Mech. B-Fluids* Vol. 41, 2013, pp. 29-45.

[6] Basak T., Anandalakshmi R., Roy M., Heatlines based natural convection analysis in tilted isosceles triangular enclosures with linearly heated inclined walls: effect of various orientations. *Int. Comm. Heat Mass Trans* Vol. 43, 2013, pp. 39-45.

[7] Bejan A., *Entropy generation through heat and fluid flow,* 2nd ed., Wiley, New York, 1994.

[8] Ilis G. G, Mobedi M., Sunden B., Effect of aspect ratio on entropy generation in a rectangular cavity with differentially heated vertical walls, *Int. Comm. Heat Mass Transfer* Vol. 35, 2008, pp. 696-703.

[9] Morsli S., Sabeur-Bendehina A., Entropy generation and natural convection in square cavities with wavy walls, *J. Appl. Mech. Tech. Phys.* Vol. 54, 2013, pp. 913-920.

[10] Bhardwaj S., Dalal A., Analysis of natural convection heat transfer and entropy generation inside porous right-angled triangular enclosure. *Int. J Heat Mass Trans.* Vol. 65, 2013, pp. 500-513.

[11] Reddy J. N., *An Introduction to the Finite Element Method* McGraw-Hill, New York, 1993.

[12] Deng Q. H., Tang G. F., Numerical visualization of mass and heat transport for conjugate natural convection/heat conduction by streamline and heatline. *Int. J. Heat Mass Tran.* vol. 45, 2002, pp. 2373-2385.

[13] Wan D. C., Patnaik B. S. V., Wei G. W., A new benchmark quality solution for the buoyancy-driven cavity by discrete singular convolution. *Numer. Heat Transfer-B* Vol. 40, 2001 pp. 199-228.